A Semi-Automatic Iterative Method for Freeze-Thaw Landslide Identification in the Permafrost Region of the Qilian Mountains

Gang Wei[1], Xiaoqing Peng[1*], Oliver W. Frauenfeld[2], Lajia Weisai[3], Chen Yang[1], Guanqun Chen[1], Panpan Wang[1], Gubu Qiumo[1], Hengxing Luo[1], Guangshang Yang[1], Xuanjia Li[1], Cuicui Mu[1]

[1]Key Laboratory of Western China's Environmental Systems (Ministry of Education), College of Earth and Environmental Sciences, Lanzhou University, Lanzhou, 730000, China
[2]Department of Geography, Texas A&M University, College Station, TX, 77843-3147, USA
[3]Qinghai Provincial General Geological and Environmental Monitoring Station (Qinghai Provincial Geological Disaster Prevention and Control Technical Guidance Center), Xining, 810000, China

Correspondence to: Xiaoqing Peng (pengxq@lzu.edu.cn)

Abstract. In permafrost regions, freeze-thaw landslides (FTLs) are a typical geological hazard that poses significant threats to environments and infrastructure at local to regional scales. However, traditional visual interpretation and also new deep learning methods still have limitations in their ability to detect and recognize FTLs at high precision, especially for hidden and small FTLs. Here we propose a semi-automatic iterative recognition method that combines InSAR surface deformation, multi-source images, and topographic factors to achieve a more accurate FTLs dataset for the Qilian Mountain permafrost region. The methodology involves four key steps: (1) acquiring surface deformation data from SBAS-InSAR with a deformation rate threshold of ≥50 mm·a⁻¹; (2) statistically analyzing topographic factors based on an existing FTLs inventory to determine initial threshold ranges; (3) extracting overlapping mask regions of these factors; and (4) verifying FTL boundaries through visual interpretation of multi-source remote sensing images and iteratively optimizing the sample database until deformation rates stabilize. Results indicate that after five iterations, 98 new FTLs were identified, primarily consisting of hidden and small-scale FTLs. The method achieved a true positive rate of 93.3%, indicating high accuracy. In addition, we found that areas with larger absolute values of deformation rate and higher seasonal deformations are more prone to FTLs. The application of this method demonstrates highly accurate and efficient FTL identification, providing a new technical approach for monitoring and assessing the FTLs.

1 Introduction

The Qilian Mountains, located in the northeastern part of the Qinghai-Tibet Plateau in China, are characterized by complex terrain and represent a typical mountain permafrost environment that is highly fragile and sensitive to climate change (Wang et al., 2006; Chen et al., 2011; Guo et al., 2024). The region has experienced significant temperature increases, leading to accelerated permafrost degradation and a frequent occurrence of geologic hazards such as freeze-thaw landslides (FTLs; Niu et al., 2016; Jackson, 2022; Deng et al., 2024). Freeze-thaw-related landslides serve as direct indicators of permafrost degradation, typically exhibiting characteristic geomorphic features including crown cracks, subvertical scarps, radial flank fractures, and transverse toe ridges, often occurring on gentle slopes with well-preserved but distinctly bounded sliding bodies displaying circular to elongated morphologies (Highland and Bobrowsky, 2008; Zhang et al., 2024). Extending the classical landslide definition (Hungr et al., 2014), we define freeze-thaw landslides (FTLs) as a distinct class of slope failures where cyclic freeze-thaw processes serve as the dominant triggering mechanism (Streletskiy et al., 2025), encompassing but are not limited to retrogressive thaw slumps (RTS) and active layer detachments (ALD). Fundamentally, these FTLs are ultimately driven by climate-induced changes including increased rainfall, rising temperatures, and deepening of the active layer, which precondition slopes for freeze-thaw destabilization (Zhang et al., 2008; Harris et al., 2009; Jin et al., 2009; Yang et al., 2022;). In recent years, the elevation at which FTLs occur has increased, rising by an average of approximately 130 m over the past decade (Chen et al., 2024). These landslides not only damage local infrastructure (e.g., roads, bridges, buildings, etc.), they

threaten the lives and properties of residents and also negatively affect the environment by destroying vegetation and altering surface runoff, which in turn affects the balance and stability of the entire ecosystem (Li et al., 2022; Liang et al., 2023). Landslide activity triggered by permafrost degradation is a significant geologic hazards that is a direct consequence of climate change (Patton et al., 2019). The volume expansion during the phase change as water freezes leads to an increase in internal

45 pore pressure and loosens the soil structure. During summer thaw and subsidence, the continuous infiltration of water leads to a decrease in both frictional resistance and shear strength, which increases the water content and weight of the soil slope, resulting in a loss of support of the subsoil layer due to softening, sliding of the superstructure, slope instability, and ultimately, the formation of FTLs (Gruber and Haeberli, 2007).

Traditional methods for identifying FTLs primarily rely on visual interpretation of optical imagery and remote sensing image

50 identification methods, combined with deep learning. Visual interpretation of optical images, as a conventional approach, benefits from interpreters' expertise in comprehensively analyzing complex terrain features, demonstrating successful identification capabilities. For example, Peng et al. (2024) used visual interpretation of optical images to compile the first inventory of hillslope thermokarst in the Qilian Mountains' permafrost region, detailing the distribution of these terrain features in the area. Similarly, Zhang et al. (2024) compiled an inventory of FTLs in the Hexi Corridor by visual interpretation, and

55 revealed the spatial distribution of landslides in the area. However, visual interpretation of optical images is limited by weather conditions, vegetation cover, and human experience, making it difficult to comprehensively and accurately identify hidden ($\Delta NDVI$>-0.1) and small (<10 ha) FTLs (Fiorucci et al., 2019). The advantage of deep learning is that it is extremely efficient and can quickly process large areas of remote sensing imagery, which greatly reduces the recognition time. Once a model is trained, the recognition of new images can be completed quickly, making it suitable for large-scale landslide surveys. For

60 example, Xia et al. (2022) utilized deep learning combined with a semi-automatic iterative approach to compile the first inventory of retrogressive thaw slumps (RTSs) along the Qinghai-Tibet Railway, significantly improving the efficiency and accuracy of RTS identification. Despite these advancements, identification accuracy still needs to be improved due to the complexity of the FTLs, and limitations arising from the sample data required for model training, which still makes the process time-consuming and laborious (Cheng et al., 2024). Therefore, the development of a semi-automatic iterative identification

65 method by combining the advantages of the two methods is an important direction for improved FTLs identification.

The occurrence of FTLs is closely related to soil freeze-thaw processes, which cause significant surface deformation that can trigger landslide hazards. Interferometric Synthetic Aperture Radar (InSAR) technology, with its all-weather, day-and-night monitoring capabilities, provides high-precision surface deformation data, offering essential support for the identification of FTLs (Du et al., 2023; Jiao et al., 2023). Combining InSAR with manual interpretation can further enhance identification

70 efficiency and accuracy. This study therefore proposes a semi-automatic iterative identification method based on InSAR, leveraging the high-precision deformation monitoring capabilities and the experiential advantages of manual interpretation to achieve efficient and accurate FTL identification. This approach not only overcomes the limitations of traditional optical imagery but also provides a new technical framework for the early identification and warning of FTLs.

2 Study Area and Data

75 ### 2.1 Study Area

The Qilian Mountains, serving as a crucial ecological barrier and water conservation area in northwestern China, are characterized by extensive permafrost that underlays approximately 50% of the region's total area (Sheng, 2020; Peng et al., 2024). The region experiences a continental alpine semi-humid mountain climate with an average annual temperature of 0.30°C (Jin et al., 2022), and precipitation primarily concentrated between May and September (Chen et al., 2018). Due to human

80 activities, climate change, earthquakes, and other factors, permafrost has been continuously degraded, triggering geologic hazards such as shallow landslides, deep-seated landslides, debris flows, and rockfalls, all of which pose direct threats to local

economies, ecosystems, and safety. The study area is located in the eastern part of the Qilian Mountains' permafrost region (99.6–101.1°E, 37.4–38.4°N; Fig. 1), with an elevation range of 3,355–4,809 m. The complex topography, variable climatic conditions, and frequent freeze-thaw cycles make it a high incidence area of FTLs (Fig. 1). The existing FTLs inventory for

85 this area can serve as the basis for the semi-automatic iterative identification method based.
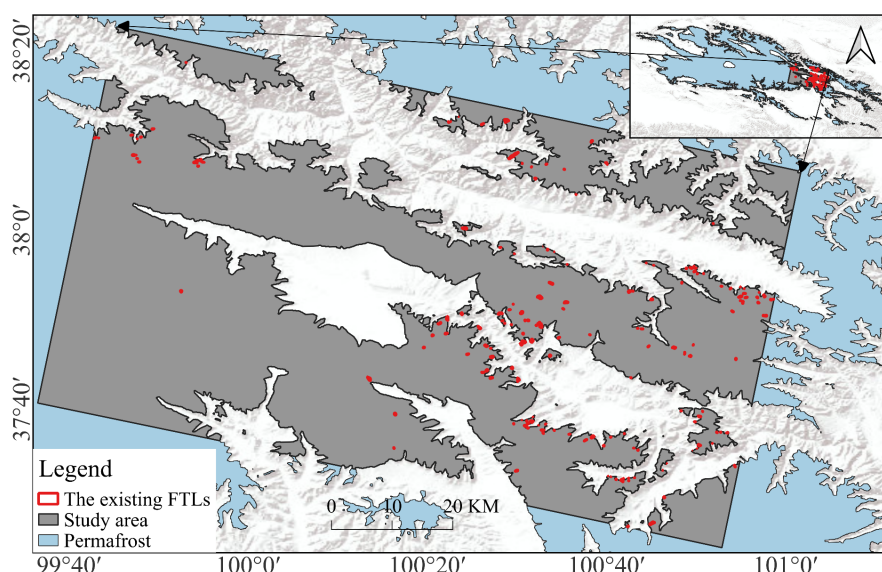
Figure 1 The study area and the existing FTLs (red points).

2.2 Data

This study utilizes multiple data sources for the identification and dynamic monitoring of FTLs, including high-resolution
90 satellite imagery, atmospheric data, digital elevation model (DEM), normalized difference vegetation index (NDVI), and field survey data.

2.2.1 Sentinel-1 SAR

The Sentinel-1A satellite is equipped with a C-band sensor (central frequency of 5.4 GHz, wavelength of approximately 5.55 cm) and has a revisit cycle of 12 days. This study uses single look complex data from the descending orbit (path 33), with an
95 image time span from March 25, 2017 to December 28, 2019, obtained from https://search.asf.alaska.edu/. A total of 82 scenes were acquired to extract time-series surface deformation data.

2.2.2 Reanalysis Data

The 5th generation of the European Centre for Medium-Range Weather Forecasts (ECMWF) reanalysis (ERA5) is used for atmospheric correction in InSAR data processing. ERA5 offers high temporal and spatial resolution, enabling precise modeling
100 of atmospheric delays and improving the accuracy of deformation time series. Data are obtained for the period from 2017 to 2019 and are critical for enhancing deformation monitoring precision (https://cds.climate.copernicus.eu/).

2.2.3 Precision Orbit Data

To improve the registration accuracy of SAR data and correct orbital errors, this study employs precision orbit data released by the Alaska Satellite Facility (ASF, https://s1qc.asf.alaska.edu/aux_poeorb/).

2.2.4 Digital Elevation Model

The DEM data, sourced from the Shuttle Radar Topography Mission (SRTM1) by the United States Geological Survey (USGS), has a spatial resolution of 30 m (Farr et al., 2007; https://www.earthdata.nasa.gov/sensors/srtm). These data are used for enhanced spectral diversity registration in Sentinel-1 terrain observation by progressive scan mode, and removal of topographic phase. Additionally, they are utilized to extract topographic factors such as elevation, slope, and aspect.

2.2.5 Normalized Difference Vegetation Index

The Landsat NDVI dataset (Qilian Mountains region, 1986–2019) is generated from Landsat 5 TM, Landsat 7 ETM+, and Landsat 8 OLI imagery, with a spatial resolution of 30 m. The dataset provides the maximum NDVI values from May to September each year (http://www.ncdc.ac.cn/). NDVI data for 2017 and 2019 are selected to calculate the NDVI change ($\Delta NDVI = NDVI_{2019} - NDVI_{2017}$) .

2.2.6 Remote Sensing Imagery

We collect multi-source remote sensing imagery, including Google Earth Pro, ESRI World Imagery, Omap, PlanetScope, and UAV images (Table 1). Google Earth Pro provides high-resolution imagery (0.6–15 m) from the QuickBird and IKONOS satellites, offering intuitive visualization of surface cover and temporal changes in the study area. ESRI World Imagery offers historical remote sensing images since 2014 with a spatial resolution of <1 m, enabling the capture of dynamic changes in surface features through time-series comparisons. Omap, also with a spatial resolution of <1 m, is sourced from the JiLin-1 satellite and provides high-resolution images from 2023 onwards. PlanetScope, acquired for July and August 2019, has a spatial resolution of 3–5 m. UAV images, with a spatial resolution of approximately 15 cm, were collected during field surveys in August 2024, supplementing satellite data. These multi-source remote sensing datasets provide multi-dimensional support for FTLs identification and dynamic monitoring.

2.2.7 Freeze-Thaw Landslides

The existing FTLs datasets are basic validation products primarily from the published (Peng et al., 2024; Zhang et al., 2024) that contain 167 FTLs and 17 RTSs in the study area.

Table 1 List of data used for manual interpretation and mapping of FTL features.

Software platform	Acquisition time	Resolution	Source/reference
Google Earth Pro	Since 1999	0.6–15 m	Quickbird, IKONOS
ESRI World Imagery	Since 2014	< 1 m	WorldView-3, WorldView-4, etc.
Omap	Since 2023	< 1 m	JiLin-1
PlanetScope	July, August 2019	3–5 m	Planet Team (2017)
UAV images	August 2024	~15 cm	Field surveys

3 Methods

3.1 Semi-Automatic Iterative Identification

3.1.1 SBAS-InSAR Processing

This study employs InSAR Scientific Computing Environment (ISCE) and MintPy software to process Sentinel-1 SAR data for extracting time-series surface deformation. We used Small Baseline Subset InSAR (SBAS-InSAR) to reduce the effects of spatiotemporal decorrelation by selecting interferograms with small spatial and temporal baselines and utilizing multi-master image datasets (Berardino et al., 2002; Usai, 2003; Lanari et al., 2004), thus effectively removing interference from low

coherence regions. Studies have shown that SBAS-InSAR performs well in monitoring surface deformation in permafrost regions (Wang et al., 2020; Peng et al., 2023).

The ISCE software is used to process SAR data, generating 395 interferograms between SAR images and their adjacent acquisitions. The orbital phase error is first corrected using precision orbit data to improve the accuracy of the interferograms.

140 Considering the impact of noise and resolution, multi-looking processing with a 2×7 window in the azimuth and range directions is applied to the generated interferograms, resulting in a resolution of approximately 30 m. The topographic phase is simulated using the DEM and removed from the interferograms. Subsequently, an adaptive spectral filter is applied to generate differential interferograms, and the Goldstein filter algorithm is employed to suppress noise in all interferograms (Goldstein and Werner, 1998). Finally, phase unwrapping is performed using the minimum cost flow method (Costantini,

145 1998). During interferogram generation, the master image is selected as March 25, 2017 with a connection number of 5, a temporal baseline limit of 60 days, and a spatial baseline limit of 150 m to ensure the quality and stability of the interferograms. Based on the interferograms generated by ISCE, the MintPy software is used to extract high-precision time-series surface deformation. The MintPy workflow includes a number of steps. First, the weights of the interferograms are determined by their coherence, and a coherence-based filtering method is used to construct the interferogram network, removing

150 interferometric pairs with poor coherence (Perissin and Wang, 2012). Next, the time-series of the original phase is resolved by minimizing phase residuals and is corrected temporally relative to the first scene of the dataset and spatially relative to a reference point. The reference point is set on the bedrock of the central ridge in the study area (37.853°N, 100.753°E), which exhibits high coherence (0.98), minimal atmospheric influence, and negligible deformation, satisfying the requirements for high-precision deformation monitoring. During time-series analysis, the minimum coherence threshold is set to 0.5 to retain

155 as many valid pixels as possible, and pixels with coherence below the threshold are masked. Additionally, to remove high-frequency noise signals, the residual root mean square error (RMSE) truncation value is set to 2.5 to further optimize the accuracy of the deformation results. The MintPy workflow also includes a tropospheric delay correction using the PyAPS method (Jolivet et al., 2014) and topographic residuals are corrected according to (Fattahi and Amelung, 2013). Finally, the weighted least squares inversion method (Zhang et al., 2019b) is applied to derive the time-series surface deformation, and the

160 results are transformed into the WGS 84 coordinate system to generate the final surface deformation data.

3.1.2 Semi-Automatic Iterative Method

The semi-automatic iterative identification method based on SBAS-InSAR proposed in this study integrates automated data processing with manual validation. It aims to utilize existing FTL datasets to preliminarily screen topographic factors and related data, rapidly locate potential landslide areas, and provide a foundation for subsequent detailed identification (Fig. 2).

165 The core workflow of this method consists of the following steps:

(1) Initial Masking and Factor Analysis

The existing FTLs dataset is used to mask topographic factors (e.g., aspect, slope, elevation), and the potential deformation area is extracted using an absolute deformation rate threshold of ≥50 mm·a^{-1}, as regions exceeding this threshold account for less than 1% of the known FTLs area. By statistically analyzing the distribution of topographic factors at landslide points, the

170 masking thresholds for each factor are determined, and single-factor mask regions are generated (Table 2). Subsequently, overlapping mask regions from these factors are extracted to obtain a relatively small but highly probable prediction range that includes the majority of potential FTLs. This step significantly narrows down the target area, providing a precise prediction region for subsequent visual interpretation of multi-source remote sensing imagery, thereby greatly improving identification efficiency and reducing unnecessary data analysis workload.

175 (2) Visual Interpretation

After completing the initial masking and determining the prediction range, manual visual interpretation is conducted using multi-source remote sensing imagery including Google Earth Pro, ESRI World Imagery, Omap, and PlanetScope. Based on

the typical characteristics of FTLs (e.g., irregular slope morphology, abnormal soil or vegetation zones, distribution and orientation of surface cracks, and potential deformation signs in shaded areas), potential landslide bodies are identified, one

180 by one, on the multi-source imagery. For areas with ambiguous or disputed boundaries, the actual boundaries and ranges of FTLs are determined by local zoom-in of high-resolution images, comparison of different time-phase images, and reference comparison with the surrounding stable areas.

(3) Iterative Optimization and Validation

Based on the visual interpretation results, the newly identified FTL regions are included in the next iteration, and the initial

185 masking thresholds are updated and optimized. Through repeated iterations, the identification results are more accurate until the surface deformation rate tends to stabilize. Because most permafrost regions are relatively stable with deformation rates ranging from −10 to 10 mm·a⁻¹ (Jiao et al., 2023), we performed five semi-automatic iterative identifications by the InSAR-based semi-automatic iterative identification method (Table 2), and finally generate accurate and reliable inventories of FTLs.
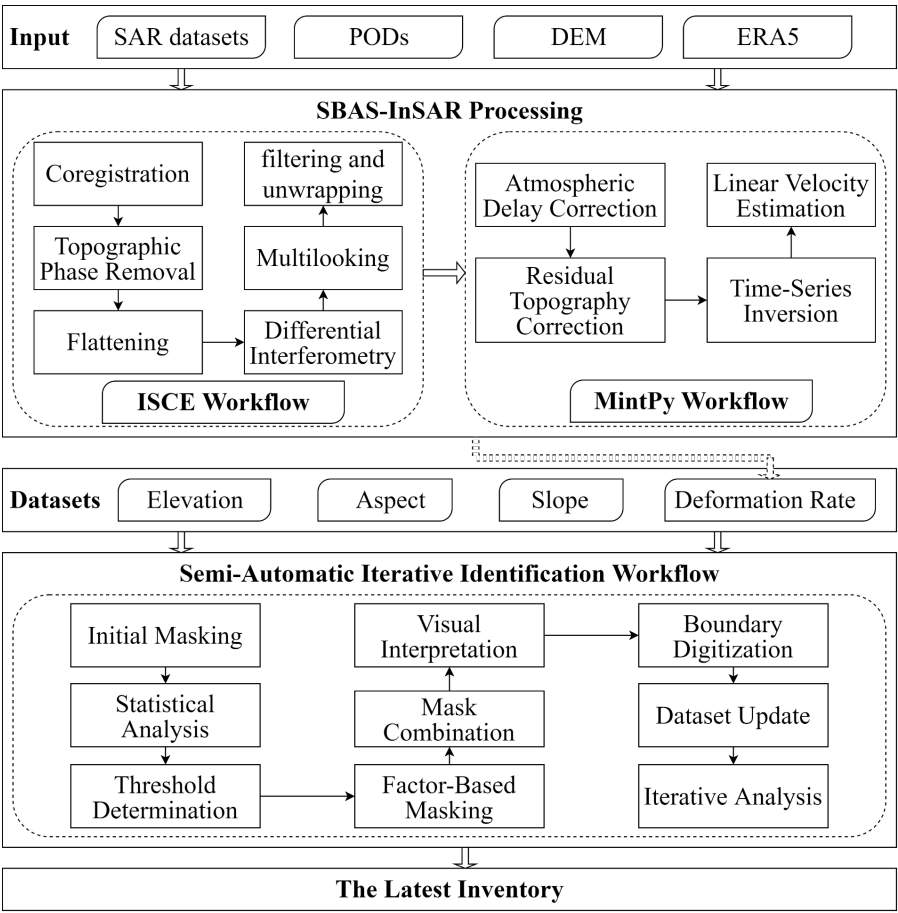
190   **Figure 2** Semi-automatic iterative identification workflow based on InSAR.

195

Table 2 Semi-automatic iterative identification method.

Iteration	Elevation (m)	Slope (°)	Aspect (°)	Deformation rate (mm·a⁻¹)	Result
1	3600-4000	1-30	0-315	abs≥50	9
2	3600-4100	1-35	0-315	abs≥40	3
3	3600-4200	1-35	0-315	abs≥30	26
4	3600-4300	1-35	0-315	abs≥20	22
5	3600-4400	1-40	0-112.5&135-360	abs≥10	38

3.2 Seasonal Deformation Modeling

Generally, the surface deformation results in permafrost regions are considered to consist of two components, long-term linear deformation rates and seasonal deformation values (Daout et al., 2017, 2020). In this study, nonlinear modeling is applied to fit the time-series surface deformation data, extracting seasonal deformation values within the study area. The nonlinear model is expressed as follows Eq. (1):

$$y(t) = a + b \cdot t + c \cdot \cos\left(\frac{2\pi}{T} \cdot t\right) + d \cdot \sin\left(\frac{2\pi}{T} \cdot t\right), \tag{1}$$

where a represents the initial deformation value; b is the long-term trend term; c and d are the amplitudes of the cosine and sine terms, respectively; T is the soil freeze-thaw cycle (assumed to be one year); and t denotes the time span with respect to the first SAR acquisition time. The seasonal deformation value can be calculated using Eq. (2):

$$A_{seasonal} = 2 \cdot \sqrt{c^2 + d^2}, \tag{2}$$

where $A_{seasonal}$ represents the seasonal deformation value of each pixel.

By integrating long-term trends and seasonal variations into the modeling process, this method enhances the accuracy of surface deformation feature extraction, providing a scientific basis for understanding surface dynamic processes in the study area.

3.3 Accuracy of Updated Inventory

To evaluate the accuracy of the InSAR-based semi-automatic iterative identification method, this study combines optical remote sensing imagery with field verification to validate the identification results. The validation process consists of two parts—optical imagery verification and field verification—as detailed below:

(1) Optical Imagery Verification

Optical remote sensing imagery verification is primarily applied to areas that are difficult to access due to complex terrain or transportation challenges. First, high-resolution optical remote sensing imagery is used to visually interpret the identified FTLs points, delineating their boundaries to assess the reliability of the identification results. Simultaneously, the optical imagery is re-examined to identify potential false negative (*FN*) points—FTLs that exist but were not detected by the method.

(2) Field Verification

Field investigations were carried out to confirm the existence and boundary ranges of the FTL points. High-resolution UAV images of the FTL points were captured to obtain detailed slope morphology and surface characteristics. Mobile photography was used to document typical features of the FTLs such as surface cracks, slope deformation, and vegetation anomalies.

(3) Precision Evaluation Calculation

Based on the statistical results from the optical imagery verification and field verification, the accuracy metrics of the identification method were calculated, including the true positive rate (*TPR*), false positive rate (*FPR*), and false negative rate (*FNR*). The specific formulas are as follows, with *N* representing the total number of FTLs (Zhang et al., 2019a):

True Positive (*TP*): when the identification result matches the actual result, the FTL point is defined as a true positive. The *TPR* is calculated as follows Eq. (3):

$$TPR = \frac{N_{TP}}{N} \cdot 100\%, \tag{3}$$

False Positive (*FP*): when an FTL point is identified but not confirmed during field investigation, it is defined as a false positive. The *FPR* is calculated as follows Eq. (4):

$$FPR = \frac{N_{FP}}{N} \cdot 100\%, \tag{4}$$

235 *False Negative* (*FN*): when an FTL point is confirmed during field investigation but not identified by the method, it is defined as a false negative. The *FNR* is calculated as follows Eq. (5):

$$FNR = \frac{N_{FN}}{N} \cdot 100\%, \tag{5}$$

4 Results

4.1 Updated Freeze-Thaw Landslides Inventory

240   Using the InSAR-based semi-automatic iterative identification method, we conducted a comprehensive and in-depth identification of FTLs in the study area. A comparison of the FTLs inventory before and after the update reveals the addition of 98 new FTL points (Fig. 3). Most FTLs are distributed along the transitional zone between permafrost and seasonal frozen ground.

The perimeter ranges from 0 to 6 km, and 65% of FTLs have a perimeter of less than 1 km (Fig. 4a). The area of FTLs ranges
245   from 0 to 60 ha, with 78% of FTLs covering less than 10 ha (Fig. 4b). FTLs predominantly occur on north-facing slopes that receive less solar radiation, with the highest concentration on northwest-facing slopes and the lowest on southeast-facing slopes (Fig. 5c). The elevation of FTLs mainly ranges from 3650 to 4000 m (Fig. 5d), influenced by freeze-thaw cycles. The slope of FTLs is concentrated between 2° and 30°, with a peak between 10° and 16°, suggesting a predominance of moderate slopes (Fig. 5e). The ΔNDVI distribution is relatively symmetrical, peaking near 0 (Fig. 5f). However, the proportion of negative
250   ΔNDVI values exceeds that of positive values, suggesting an overall trend of vegetation degradation.
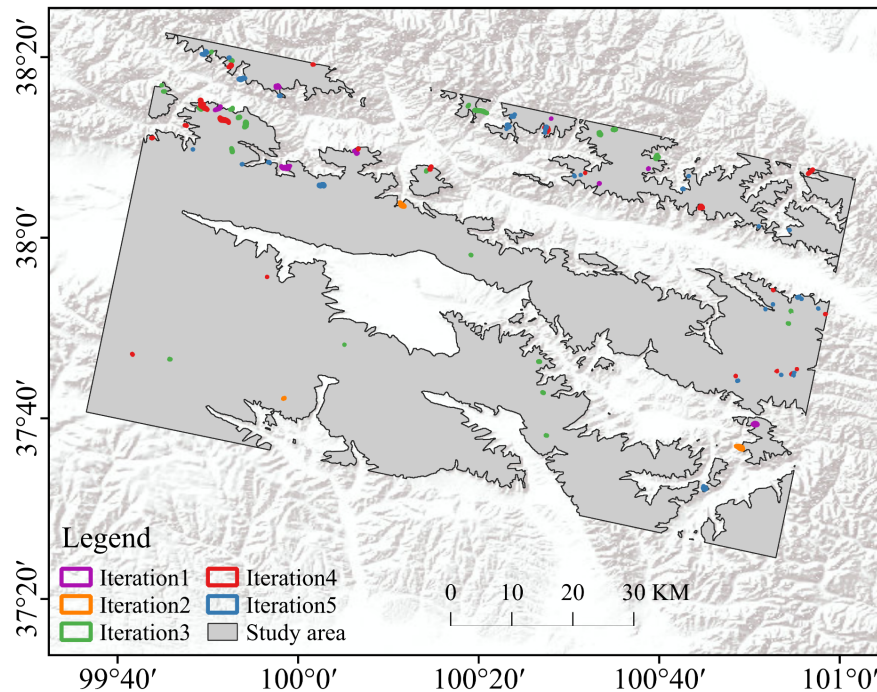
Figure 3 The spatial distribution of new freeze-thaw landslide in each iteration.
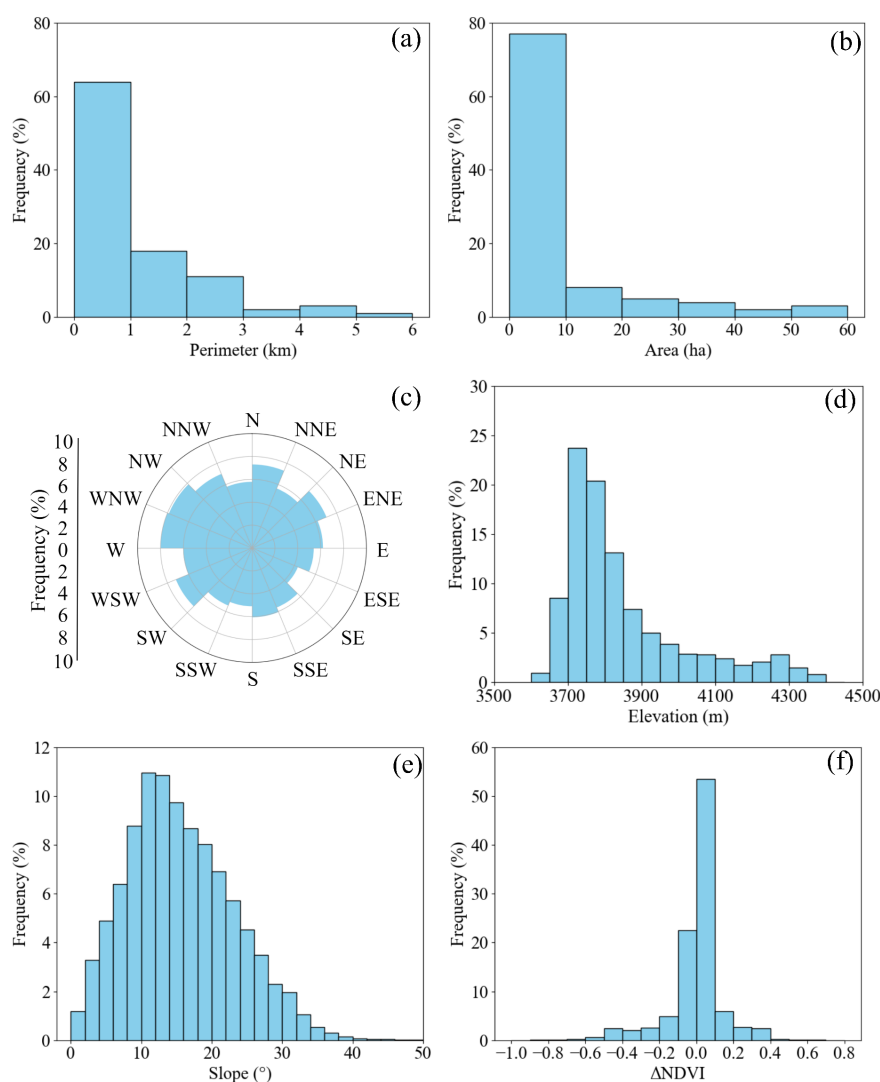
Figure 4 The geometric characteristics and terrain and vegetation factors frequencies of the newly identified FTLs. (a) Histogram showing the perimeter sizes of all FTLs; (b) histogram showing the sizes of all FTLs; (c) polar plot of the aspect distribution; (d) histogram of elevation distribution; (e) histogram of slope distribution; and (f) histogram of ΔNDVI distribution.

4.2 Inventory Validation

To assess the reliability of the InSAR-based semi-automatic iterative identification method, we selected 15 FTLs in three regions to verify the accuracy of the inventory (Fig. 5). Field investigations were conducted in August 2024 in region b and Region c. Region a was verified using optical imagery, with all 8 FTLs identified as *TP*. Region b was verified through field surveys, with 1 FTL identified as *TP*. Region c combined optical imagery verification and field surveys, involving 6 FTLs of which 5 were verified in the field and one (OID95) was verified using optical imagery. During the field investigation in region c, one *FN* FTL (OID59) was discovered. Through comparison of multi-source remote sensing imagery, we found that although this FTL exhibited significant surface deformation and was in the potential landslide range, a lack of noticeable vegetation

265   cover changes led to its misidentification. The final calculated validation metrics of our method show a *TPR* of 93.3%, *FPR*

of 0%, and *FNR* 6.7%, which demonstrates the high overall identification accuracy of the method.
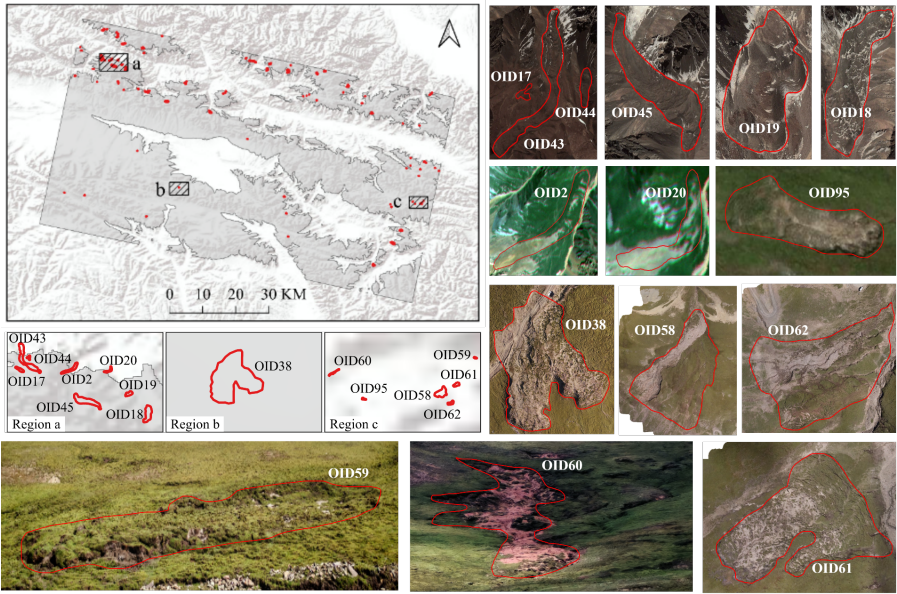
Figure 5 Regions a–c were selected to evaluate the inventory accuracy based on optical imagery (OID2, OID17, OID18, OID19, OID20, OID43, OID44, OID45, and OID95), field verification using UAV images (OID38, OID58, OID61, and OID62), and mobile photography

270   (OID59 and OID60).

4.3 Surface Deformation of Freeze-Thaw Landslides

Across the whole study area, the deformation rates range from −155 to 78 mm·a⁻¹. Most of the area (73%) experienced

deformation rates within ±10 mm·a⁻¹, indicating relative stability (Fig. 6a). The seasonal deformation ranged from 0 to 45 mm,

with 77% of the area showing seasonal deformation between 0 and 10 mm, further confirming the overall surface stability in

275   the study area (Fig. 6b). In regions where the absolute deformation rate exceeds 15 mm·a⁻¹, the proportion of FTLs is higher

than that of the overall study area (Fig. 7a). The trend is particularly pronounced in areas with absolute deformation rates

greater than 20 mm·a⁻¹, where the frequency of FTLs substantially increases. Similarly, in regions with seasonal deformation

values between 9 and 21 mm (Fig. 7b), the proportion of FTLs is also higher than that of the overall study area.
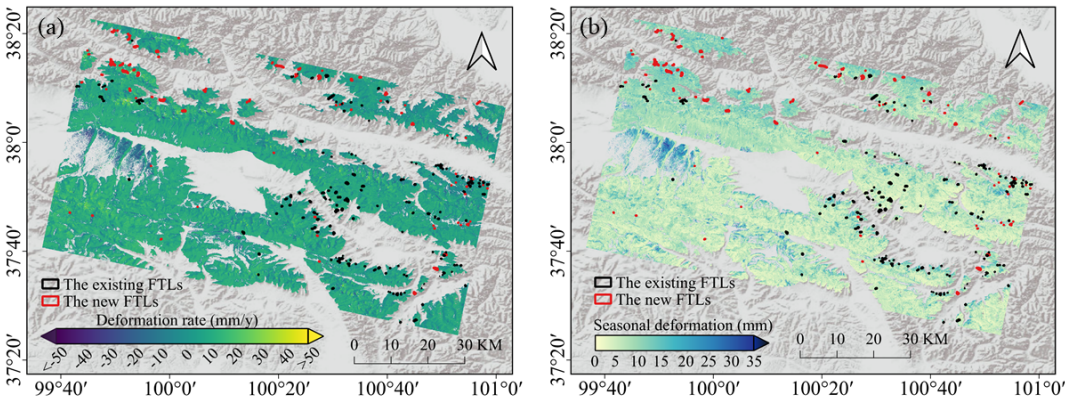
280   **Figure 6** Deformation characteristics of the study area: (a) surface deformation rate (−155 to 78 mm·a⁻¹) and (b) seasonal deformation
amplitude (0–45 mm).
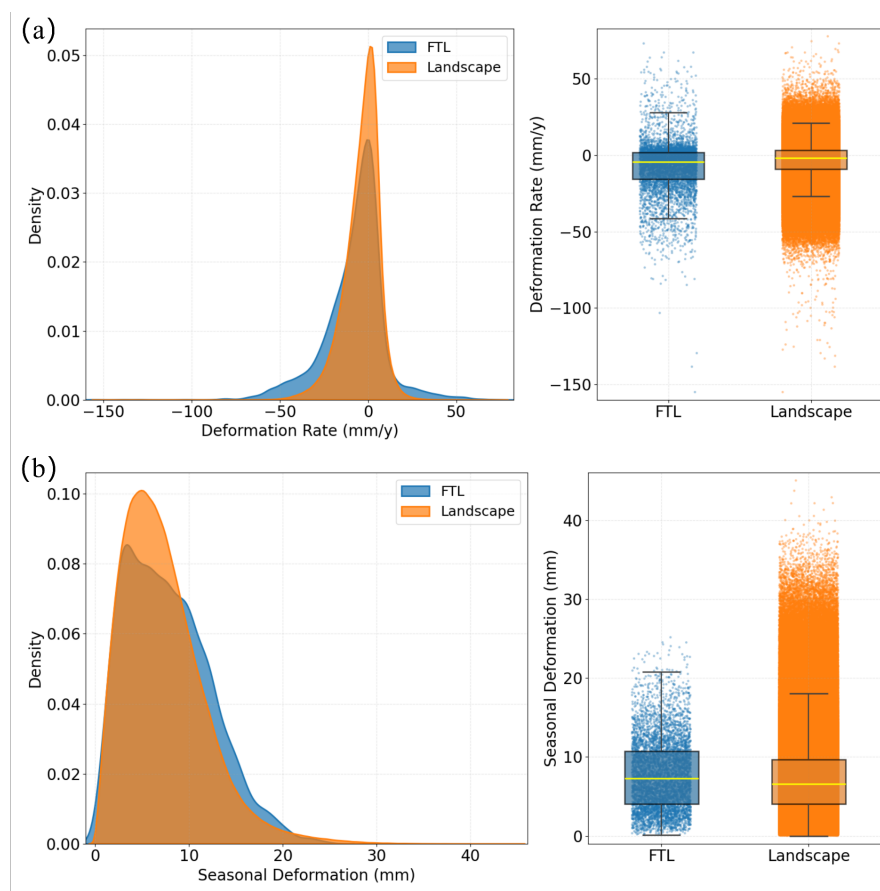
Figure 7 Distribution of deformation parameters: (a) deformation rate and (b) seasonal deformation. Left panels show probability density distributions and right panels present scatter point distributions with overlain boxplots.

5 Discussion

5.1 Advantages of the Proposed Method

The InSAR-based semi-automatic iterative identification method proposed in this study demonstrates significant advantages in the identification of FTLs. First, by integrating the high-precision deformation monitoring capabilities of InSAR technology with the visual interpretation of multi-source remote sensing imagery, we significantly improve the accuracy of FTL identification. Compared to traditional visual interpretation methods using optical imagery (Xia et al., 2022; Peng et al., 2024; Zhang et al., 2024), our new approach effectively overcomes interference from weather conditions and vegetation cover, particularly showing strong ability in identifying hidden and small-scale FTLs (Du et al., 2023; Jiao et al., 2023). Second, the iterative optimization approach of our method progressively narrows the prediction range, reduces incorrect identification rates, and ultimately generates a highly reliable FTL inventory (Almudevar and De Arruda, 2012). Additionally, the method exhibits notable efficiency advantages. By extracting regions with higher surface deformation rates to narrow the prediction range, it significantly reduces the time required for FTL identification, thereby making it suitable for large-scale FTL surveys.

5.2 Limitations and Challenges

Although the proposed method demonstrates high accuracy and efficiency in identifying FTLs, it still faces limitations. For instance, he method relies heavily on the temporal coverage, data quality, and resolution of InSAR. Some FTLs occurred

300   outside the time range covered by the InSAR data, making it difficult to identify both new and old FTLs. InSAR technology
        encounters issues such as atmospheric delays and phase noise (Nico et al., 2011). Although these issues are mitigated through
        atmospheric correction and filtering, they cannot be entirely eliminated, potentially affecting the accuracy of deformation
        monitoring (Li et al., 2019).

        Additionally, the threshold settings in the iterative identification process are based on statistical analysis of existing landslide
305   characteristics, which may not fully encompass the entire range of features for all FTLs, particularly those with atypical
        geomorphologic or kinematic characteristics (Kim and Park, 2020). While the manual visual interpretation step leverages the
        expertise of professionals to accurately assess complex areas, it is not entirely free from subjectivity (Ramli et al., 2010).
        Differences in interpretation among analysts regarding the same image features may lead to discrepancies in boundary
        delineation and landslide type classification.

310   6 Conclusions

        Due to the limited accuracy of traditional visual interpretation methods using optical imagery and deep learning-based remote
        sensing techniques, this study introduces surface deformation rate as a key factor and proposes a semi-automatic iterative
        identification method based on InSAR. This method effectively addresses the challenges of identifying hidden and small-scale
        FTLs, achieving a true positive rate of 93.3% with the updated inventory that also adds 98 new FTL points. Areas with higher
315   absolute rates of deformation (especially greater than 20 mm·a^{-1}) and higher values of seasonal deformation (greater than 10
        mm) are more susceptible to FTLs compared to stable terrain. The research characterizes the spatial predisposition of FTLs,
        showing pronounced aggregation on northwest aspects (receiving minimal solar radiation), in the 3650–4000 m altitudinal belt
        (most active freeze-thaw cycle), and areas exhibiting vegetation degradation (ΔNDVI<0). These parameters, when integrated
        with surface deformation rates ($\geq$10 mm·a^{-1}), establish diagnostic environmental thresholds for permafrost landslide
320   susceptibility.

        Although the introduction of surface deformation factors improves identification accuracy to some extent, the method still has
        limitations. These include the limited temporal coverage of InSAR, a strong dependence on data quality and resolution, and
        the inherent subjectivity of manual visual interpretation. Therefore, future research could explore combining InSAR-derived
        surface deformation factors with deep learning-based semi-automatic iterative identification methods to further enhance
325   efficiency and performance.

Data availability

        The Sentinel-1A data can be obtained from ASF (https://search.asf.alaska.edu/); ERA5 data can be obtained from CDS
        (https://cds.climate.copernicus.eu/); POD data can be accessed through the ASF (https://s1qc.asf.alaska.edu/aux_poeorb/);
        DEM data can be accessed through NASA (https:// www.earthdata.nasa.gov/sensors/srtm, Farr et al., 2007); The Landsat
330   NDVI dataset are available from the NCDC (http://www.ncdc.ac.cn/); ESRI World Imagery can be accessed through ESRI
        Wayback Imagery at https://livingatlas.arcgis.com/wayback/; Some JiLin-1 imagery is also available online through the Omap
        software (https://www.ovital.com/283-2/, JiLin-1); High-resolution 3D satellite imagery of the Qilian Mountains region can
        be viewed in Google Earth Pro software; The PlanetScope CubeSat images are copyrighted by Planet Labs Inc., restricted by
        commercial policies and are not open to the public; The existing FTLs datasets accessible through Peng et al. (2024) and Zhang
335   et al. (2024), TPDC, https://data.tpdc.ac.cn/; The study data are available from the corresponding author upon request
        (pengxq@lzu.edu.cn).

Author contribution

GW and XP planned the campaign; GW, GY, HL, GQ, CY, PW and LW conducted the field work; GW analyzed the data and wrote the manuscript draft; XP, CM and OWF reviewed and edited the manuscript.

340 **Competing interests**

The authors declare that they have no conflict of interest.

Disclaimer

Publisher's note: Copernicus Publications remains neutral with regard to jurisdictional claims made in the text, published maps, institutional affiliations, or any other geographical representation in this paper. While Copernicus Publications makes every
345 effort to include appropriate place names, the final responsibility lies with the authors.

Acknowledgements

We thank all data providers and organizations for use of their products.

Financial support

This work was supported by the Gansu Province Science and Technology Major Special Projects (Grant No.25ZDFA013),
350 National Natural Science Foundation of China (Grant No. 42161160328) and the Science Fund for Distinguished Young Scholars of Gansu Province (Grant No.25JRRA633).

References

Almudevar, A. and De Arruda, E. F.: Optimal Approximation Schedules for a Class of Iterative Algorithms, With an Application to Multigrid Value Iteration, IEEE Trans. Automat. Contr., 57, 3132–3146,
355 https://doi.org/10.1109/TAC.2012.2203053, 2012.

Berardino, P., Fornaro, G., Lanari, R., and Sansosti, E.: A new algorithm for surface deformation monitoring based on small baseline differential SAR interferograms, IEEE Trans. Geosci. Remote Sensing, 40, 2375–2383, https://doi.org/10.1109/TGRS.2002.803792, 2002.

Chen, F., Yuan, Y., and Wei, W.: Climatic response of Picea crassifolia tree-ring parameters and precipitation reconstruction
360 in the western Qilian Mountains, China, Journal of Arid Environments, 75, 1121–1128, https://doi.org/10.1016/j.jaridenv.2011.06.010, 2011.

Chen, J., Zhang, J., Wu, T.-H., Liu, L., Zhang, F.-Y., Hao, J.-M., Huang, L.-C., Wu, X.-D., Wang, P.-L., Xia, Z.-X., Zhu, X.-F., and Lou, P.-Q.: Elevation-dependent shift of landslide activity in mountain permafrost regions of the Qilian Mountains, Advances in Climate Change Research, 15, 1067–1077, https://doi.org/10.1016/j.accre.2024.11.003, 2024.

365 Chen, R., Han, C., Liu, J., Yang, Y., Liu, Z., Wang, L., and Kang, E.: Maximum precipitation altitude on the northern flank of the Qilian Mountains, northwest China, Hydrology Research, 49, 1696–1710, https://doi.org/10.2166/nh.2018.121, 2018.

Cheng, G., Wang, Z., Huang, C., Yang, Y., Hu, J., Yan, X., Tan, Y., Liao, L., Zhou, X., Li, Y., Hussain, S., Faisal, M., and Li, H.: Advances in Deep Learning Recognition of Landslides Based on Remote Sensing Images, Remote Sensing, 16, 1787, https://doi.org/10.3390/rs16101787, 2024.

370   Costantini, M.: A novel phase unwrapping method based on network programming, IEEE Trans. Geosci. Remote Sensing, 36, 813–821, https://doi.org/10.1109/36.673674, 1998.

Daout, S., Doin, M., Peltzer, G., Socquet, A., and Lasserre, C.: Large-scale InSAR monitoring of permafrost freeze-thaw cycles on the Tibetan Plateau, Geophysical Research Letters, 44, 901–909, https://doi.org/10.1002/2016GL070781, 2017.

Daout, S., Dini, B., Haeberli, W., Doin, M.-P., and Parsons, B.: Ice loss in the Northeastern Tibetan Plateau permafrost as seen

375   by 16 yr of ESA SAR missions, Earth and Planetary Science Letters, 545, 116404, https://doi.org/10.1016/j.epsl.2020.116404, 2020.

Deng, H., Zhang, Z., and Wu, Y.: Accelerated permafrost degradation in thermokarst landforms in Qilian Mountains from 2007 to 2020 observed by SBAS-InSAR, Ecological Indicators, 159, 111724, https://doi.org/10.1016/j.ecolind.2024.111724, 2024.

380   Du, J., Li, Z., Song, C., Zhu, W., Ji, Y., Zhang, C., Chen, B., and Su, S.: InSAR-Based Active Landslide Detection and Characterization Along the Upper Reaches of the Yellow River, IEEE J. Sel. Top. Appl. Earth Observations Remote Sensing, 16, 3819–3830, https://doi.org/10.1109/JSTARS.2023.3263003, 2023.

Farr, T. G., Rosen, P. A., Caro, E., Crippen, R., Duren, R., Hensley, S., Kobrick, M., Paller, M., Rodriguez, E., Roth, L., Seal, D., Shaffer, S., Shimada, J., Umland, J., Werner, M., Oskin, M., Burbank, D., and Alsdorf, D.: The Shuttle Radar Topography

385   Mission, Reviews of Geophysics, 45, 2005RG000183, https://doi.org/10.1029/2005RG000183, 2007.

Fattahi, H. and Amelung, F.: DEM Error Correction in InSAR Time Series, Geoscience and Remote Sensing, IEEE Transactions on, 51, 4249–4259, https://doi.org/10.1109/TGRS.2012.2227761, 2013.

Fiorucci, F., Ardizzone, F., Mondini, A. C., Viero, A., and Guzzetti, F.: Visual interpretation of stereoscopic NDVI satellite images to map rainfall-induced landslides, Landslides, 16, 165–174, https://doi.org/10.1007/s10346-018-1069-y, 2019.

390   Goldstein, R. M. and Werner, C. L.: Radar interferogram filtering for geophysical applications, Geophysical Research Letters, 25, 4035–4038, https://doi.org/10.1029/1998GL900033, 1998.

Gruber, S. and Haeberli, W.: Permafrost in steep bedrock slopes and its temperature-related destabilization following climate change, J. Geophys. Res., 112, 2006JF000547, https://doi.org/10.1029/2006JF000547, 2007.

Guo, Y., Zhang, Z., and Dai, F.: Freeze-thaw landslide susceptibility assessment and its future development on the seasonally

395   frozen ground of the Qinghai-Tibet Plateau under warming-humidifying climate, Cold Regions Science and Technology, 227, 104293, https://doi.org/10.1016/j.coldregions.2024.104293, 2024.

Harris, C., Arenson, L. U., Christiansen, H. H., Etzelmüller, B., Frauenfelder, R., Gruber, S., Haeberli, W., Hauck, C., Hölzle, M., Humlum, O., Isaksen, K., Kääb, A., Kern-Lütschg, M. A., Lehning, M., Matsuoka, N., Murton, J. B., Nötzli, J., Phillips, M., Ross, N., Seppälä, M., Springman, S. M., and Vonder Mühll, D.: Permafrost and climate in Europe: Monitoring and

400   modelling thermal, geomorphological and geotechnical responses, Earth-Science Reviews, 92, 117–171, https://doi.org/10.1016/j.earscirev.2008.12.002, 2009.

Highland, L.M., Bobrowsky, P., 2008. The Landslide Handbook - A Guide to Understanding Landslides (Report No. 1325), Circular. https://doi.org/10.3133/cir1325

Hungr, O., Leroueil, S., Picarelli, L., 2014. The Varnes classification of landslide types, an update. Landslides 11, 167–194.

405   https://doi.org/10.1007/s10346-013-0436-y

Jackson, M.: Snow and Ice-Related Hazards, Risks, and Disasters. 2nd Edition. Edited by Wilfried Haeberli and Colin Whiteman, Mountain Research and Development, 42, https://doi.org/10.1659/mrd.mm272.1, 2022.

Jiao, Z., Xu, Z., Guo, R., Zhou, Z., and Jiang, L.: Potential of Multi-temporal InSAR for Detecting Retrogressive Thaw Slumps: A Case of the Beiluhe Region of the Tibetan Plateau, Int J Disaster Risk Sci, 14, 523–538, https://doi.org/10.1007/s13753-

410   023-00505-x, 2023.

Jin, H., He, R., Cheng, G., Wu, Q., Wang, S., Lü, L., and Chang, X.: Changes in frozen ground in the Source Area of the Yellow River on the Qinghai–Tibet Plateau, China, and their eco-environmental impacts, Environ. Res. Lett., 4, 045206, https://doi.org/10.1088/1748-9326/4/4/045206, 2009.

Jin, H., Li, X., Frauenfeld, O. W., Zhao, Y., Chen, C., Du, R., Du, J., and Peng, X.: Comparisons of statistical downscaling
415 methods for air temperature over the Qilian Mountains, Theor Appl Climatol, 149, 893–896, https://doi.org/10.1007/s00704-022-04081-w, 2022.

Jolivet, R., Agram, P. S., Lin, N. Y., Simons, M., Doin, M., Peltzer, G., and Li, Z.: Improving InSAR geodesy using Global Atmospheric Models, JGR Solid Earth, 119, 2324–2341, https://doi.org/10.1002/2013JB010588, 2014.

Kim, D. and Park, D.: Element-Wise Adaptive Thresholds for Learned Iterative Shrinkage Thresholding Algorithms, IEEE
420 Access, 8, 45874–45886, https://doi.org/10.1109/ACCESS.2020.2978237, 2020.

Lanari, R., Lundgren, P., Manzo, M., and Casu, F.: Satellite radar interferometry time series analysis of surface deformation for Los Angeles, California, Geophysical Research Letters, 31, 2004GL021294, https://doi.org/10.1029/2004GL021294, 2004.

Li, Y., Qin, X., Liu, Y., Jin, Z., Liu, J., Wang, L., and Chen, J.: Evaluation of Long-Term and High-Resolution Gridded Precipitation and Temperature Products in the Qilian Mountains, Qinghai–Tibet Plateau, Front. Environ. Sci., 10, 906821,
425 https://doi.org/10.3389/fenvs.2022.906821, 2022.

Li, Z., Cao, Y., Wei, J., Duan, M., Wu, L., Hou, J., and Zhu, J.: Time-series InSAR ground deformation monitoring: Atmospheric delay modeling and estimating, Earth-Science Reviews, 192, 258–284, https://doi.org/10.1016/j.earscirev.2019.03.008, 2019.

Liang, L., Sun, Y., Guan, Q., Pan, N., Du, Q., Mi, J., and Shan, Y.: Projection of landscape ecological risk and exploration of
430 terrain effects in the Qilian Mountains, China, Land Degrad Dev, 34, 4575–4593, https://doi.org/10.1002/ldr.4794, 2023.

Nico, G., Tome, R., Catalao, J., and Miranda, P. M. A.: On the Use of the WRF Model to Mitigate Tropospheric Phase Delay Effects in SAR Interferograms, IEEE Trans. Geosci. Remote Sensing, 49, 4970–4976, https://doi.org/10.1109/TGRS.2011.2157511, 2011.

Niu, F., Luo, J., Lin, Z., Fang, J., and Liu, M.: Thaw-induced slope failures and stability analyses in permafrost regions of the
435 Qinghai-Tibet Plateau, China, Landslides, 13, 55–65, https://doi.org/10.1007/s10346-014-0545-2, 2016.

Patton, A. I., Rathburn, S. L., and Capps, D. M.: Landslide response to climate change in permafrost regions, Geomorphology, 340, 116–128, https://doi.org/10.1016/j.geomorph.2019.04.029, 2019.

Peng, X., Yang, G., Frauenfeld, O. W., Li, X., Tian, W., Chen, G., Huang, Y., Wei, G., Luo, J., Mu, C., and Niu, F.: The first hillslope thermokarst inventory for the permafrost region of the Qilian Mountains, Earth Syst. Sci. Data, 16, 2033–2045,
440 https://doi.org/10.5194/essd-16-2033-2024, 2024.

Perissin, D. and Wang, T.: Repeat-Pass SAR Interferometry With Partially Coherent Targets, IEEE Trans. Geosci. Remote Sensing, 50, 271–280, https://doi.org/10.1109/TGRS.2011.2160644, 2012.

Ramli, M. F., Yusof, N., Yusoff, M. K., Juahir, H., and Shafri, H. Z. M.: Lineament mapping and its application in landslide hazard assessment: a review, Bull Eng Geol Environ, 69, 215–233, https://doi.org/10.1007/s10064-009-0255-5, 2010.

445 Ran, Y., Li, X., Cheng, G., Nan, Z., Che, J., Sheng, Y., Wu, Q., Jin, H., Luo, D., Tang, Z., and Wu, X.: Mapping the permafrost stability on the Tibetan Plateau for 2005–2015, Sci. China Earth Sci., 64, 62–79, https://doi.org/10.1007/s11430-020-9685-3, 2021.

Sheng, 2020. Map of permafrost distribution in the Qilian Mountains. National Tibetan Plateau Data Center. https://doi.org/10.11888/Geocry.tpdc.270456

450 Streletskiy, D.A., Maslakov, A., Grosse, G., Shiklomanov, N.I., Farquharson, L., Zwieback, S., Iwahana, G., Bartsch, A., Liu, L., Strozzi, T., Lee, H., Debolskiy, M.V., 2025. Thawing permafrost is subsiding in the Northern Hemisphere—review and perspectives. Environ. Res. Lett. 20, 013006. https://doi.org/10.1088/1748-9326/ada2ff

Usai, S.: A least squares database approach for SAR interferometric data, IEEE Trans. Geosci. Remote Sensing, 41, 753–760, https://doi.org/10.1109/TGRS.2003.810675, 2003.

455   Wang, G., Li, Y., Wu, Q., and Wang, Y.: Impacts of permafrost changes on alpine ecosystem in Qinghai-Tibet Plateau, SCI CHINA SER D, 49, 1156–1169, https://doi.org/10.1007/s11430-006-1156-0, 2006.

Wang, J., Wang, C., Zhang, H., Tang, Y., Zhang, X., and Zhang, Z.: Small-Baseline Approach for Monitoring the Freezing and Thawing Deformation of Permafrost on the Beiluhe Basin, Tibetan Plateau Using TerraSAR-X and Sentinel-1 Data, Sensors, 20, 4464, https://doi.org/10.3390/s20164464, 2020.

460   Xia, Z., Huang, L., Fan, C., Jia, S., Lin, Z., Liu, L., Luo, J., Niu, F., and Zhang, T.: Retrogressive thaw slumps along the Qinghai–Tibet Engineering Corridor: a comprehensive inventory and their distribution characteristics, Earth Syst. Sci. Data, 14, 3875–3887, https://doi.org/10.5194/essd-14-3875-2022, 2022.

Yang, J., Wu, G., Jiao, J., Dyck, M., and He, H.: Freeze-thaw induced landslides on grasslands in cold regions, CATENA, 219, 106650, https://doi.org/10.1016/j.catena.2022.106650, 2022.

465   Zhang, J., Wang, Q., and Su, F.: Automatic Extraction of Offshore Platforms in Single SAR Images Based on a Dual-Step-Modified Model, https://doi.org/10.3390/s19020231, 2019a.

Zhang, J., Chen, J., Li, C., Lu, W., Hao, J., Niu, P., Li, K., Ma, S., and Yuan, R.: Landslides along the Engineering Corridors in the Northeastern Margin of the Qinghai-Tibet Plateau of China: Comprehensive Inventory and Mechanism Analysis, Landslides, 21, 3049–3067, https://doi.org/10.1007/s10346-024-02341-6, 2024.

470   Zhang, T., Barry, R. G., Knowles, K., Heginbottom, J. A., and Brown, J.: Statistics and characteristics of permafrost and ground-ice distribution in the Northern Hemisphere, Polar Geography, 31, 47–68, https://doi.org/10.1080/10889370802175895, 2008.

Zhang, Y., Heresh, F., and Falk, A.: Small baseline InSAR time series analysis: Unwrapping error correction and noise reduction, Computers & Geosciences, 133, 104331, https://doi.org/10.1016/j.cageo.2019.104331, 2019b.